Supplement of "Long-term vertical characterisation of the North Atlantic subtropical atmosphere using lidar and radiosondes profiles"

Barreto et al.

S1 Atmospheric layer's description

The correct identification of the different atmospheric layers is crucial to the characterisation of the vertical structure of the lower troposphere. The MBL is important because it will define the sea-salt aerosol layer. Its height is determined by two different and independent techniques: lidar and radiosondes.

Using the lidar observations described in Sect. 3.2, we identify the MBL height as the altitude at which the strongest decrease in the aerosol backscatter signal is measured and thus it matches the top of the marine-aerosol-laden layer (Baars et al., 2008). Here we use the gradient method (Endlich et al., 1979), which determines the MBL height as the altitude where the minimum of the first derivative of the range corrected signal is found.

MBL height determination with radiosondes (described in Sect. 3.3) relies on the existence of a capping temperature inversion at the top of this layer which limits the vertical transport of heat, humidity and aerosols. We identify this inversion by means of the temperature lapse rate between the altitude levels z_i and z_j ($\Gamma_{i,j}$), calculated at each level according to Carrillo et al. (2016) and references therein. Following these authors, MBL and other inversion layers (as, for example, the inversion layer associated with the SAL's top) are detected when the temperature lapse rate shows positive values; isothermal layers are discarded.

MBL height determination can be difficult due to its evolution and complex internal structure and because of the presence of multiple aerosol layers. which can lead to an under- or overestimation of the MBL height in the case of lidar data (Wiegner et al., 2006; Ansmann, 2006; Martucci et al., 2007; Zhong et al., 2020).

The thickness of the MBL, determined independently with lidar and radiosonde yields fairly consistent results throughout the year (see Fig. S1 and Table 1). These results also show an MBL height seasonality captured by the radiosondes, with a slight maximum in December-January (1.6 km in December) and a slight minimum in summer (1.1 km in August). This seasonal variability is driven by large-scale subsidence processes (Johnson et al., 1995; Rouault et al., 2000; Von Engeln et al., 2005; Carrillo et al., 2016). However, some differences appear in the case of the seasonal MBL's top retrieved from lidar data. This instrument does not capture the expected seasonal cycle, yielding differences with radiosondes up to 300 m with the radiosondes MBL top and 400 m for the base. The greatest differences between lidar and radiosondes are found in winter (in December and January, see Table 1) when the dust transport is confined within the first two kilometres.
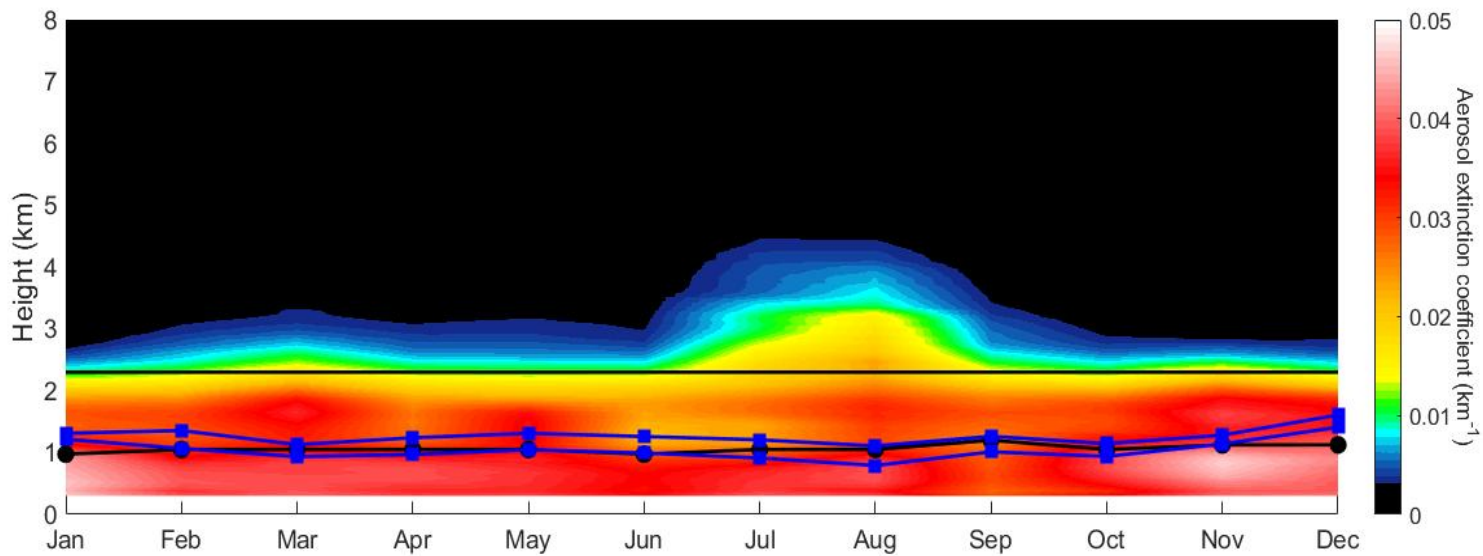
Figure S1. Aerosol extinction coefficient (α) and MBL monthly mean values obtained in the period 2007-2018. The horizontal black solid line represents the IZO level. Black circles represent the monthly mean MBL height retrieved from lidar, and the blue squares represent the top and base of the MBI, respectively, obtained from radiosondes.

Table 1. Statistics of monthly MBI height in km retrieved by the lidar (MBI_L) and the radiosondes (top as MBI_R^{top} and base as MBI_R^{base}). Monthly mean α values (in km^{-1}) at SCO (α_{SCO}) and IZO (α_{IZO}) are included. Standard deviation is also included when applicable.

| Month	MBI_L (km)	MBI_R^{top} (km)	MBI_R^{base} (km)	α_{SCO} (km^{-1})	α_{IZO} (km^{-1})
January	0.975 (0.412)	1.312 (0.451)	1.216 (0.462)	0.046 (0.064)	0.008 (0.013)
February	1.050 (0.401)	1.356 (0.527)	1.067 (0.513)	0.039 (0.049)	0.010 (0.032)
March	1.050 (0.384)	1.129 (0.491)	0.934 (0.489)	0.040 (0.049)	0.014 (0.046)
April	1.050 (0.402)	1.239 (0.401)	0.969 (0.411)	0.038 (0.049)	0.010 (0.060)
May	0.975 (0.424)	1.312 (0.419)	1.046 (0.420)	0.038 (0.034)	0.010 (0.036)
June	1.050 (0.391)	1.260 (0.362)	0.993 (0.363)	0.035 (0.037)	0.009 (0.039)
July	1.050 (0.436)	1.206 (0.299)	0.912 (0.314)	0.040 (0.038)	0.018 (0.043)
August	1.050 (0.462)	1.107 (0.301)	0.790 (0.303)	0.038 (0.046)	0.023 (0.050)
September	1.200 (0.431)	1.263 (0.289)	1.012 (0.389)	0.029 (0.033)	0.012 (0.024)
October	1.050 (0.473)	1.146 (0.546)	0.937 (0.522)	0.034 (0.045)	0.009 (0.031)
November	1.125 (0.499)	1.282 (0.571)	1.139 (0.551)	0.041 (0.043)	0.013 (0.033)
December	1.125 (0.461)	1.609 (0.492)	1.410 (0.466)	0.042 (0.055)	0.009 (0.024)

S2 Aerosol optical properties

Monthly average values of aerosol extinction at 523 nm (α), obtained from 33018 lidar vertical profiles in the period 2007-2018, are shown in Table 1, while its vertical evolution throughout the year is shown in Fig. S1. In SCO, maximum α values at lower levels, below 1 km height, are observed in winter, mainly from November to January (0.041 - 0.046 km^{-1}), as a result of the low-altitude westwards dust transport. Two peaks of lower intensity are observed in March and July/August ($\alpha \sim 0.040$ km^{-1}). However, very clean conditions ($\alpha \leq 0.010$ km^{-1}) are observed at upper levels (above 2 km, the altitude of IZO) throughout the year except for the dustiest months (July and August, up to 0.023 km^{-1}) and the transition months (March, September and November, from 0.012 km^{-1} to 0.014 km^{-1}).

These results show a vertical distribution of aerosols with a marked seasonal behaviour in which there are two predominant layers: the lower layer (L_1), from sea level to the MBL's top, and the upper layer (L_2), above the MBL, which can be located in the FT or strongly affected by the African CBL. The seasonal characterisation of L_1 and L_2 by means of the AOD calculated by integrating the aerosol extinction vertical profiles (α) over the two layers is shown in Fig. S2. Relative stable AOD values are observed in layer L_1, with maximum values higher than 0.1 only observed in January and December. Low AOD is observed
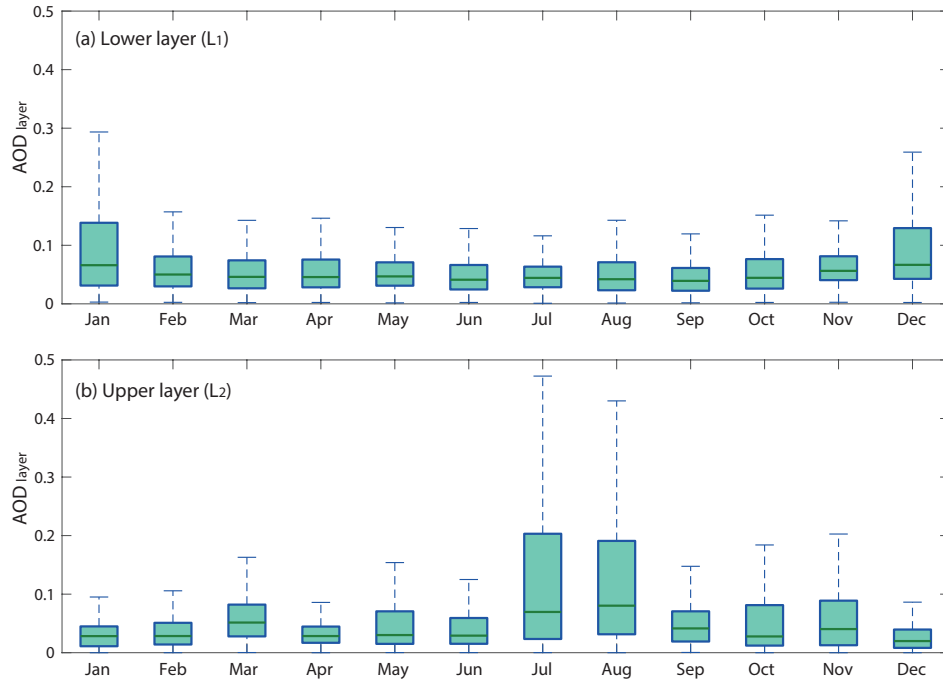
Figure S2. Boxplot of the monthly AOD in each layer retrieved by integrating the lidar extinction vertical profiles (α) in: (a) the lower layer L_1 (from surface to the MBI); (b) the upper layer L_2 (from the MBI upwards). The central horizontal green line indicates the median, and the bottom and top edges of the box indicate the 25th and 75th percentiles, respectively. The whiskers extend to the most extreme data points (outliers not shown). The percentage contribution of L_1 and L_2 to the total AOD is also included in the upper part of the graphs.

in L_2, except for July and August, and two secondary peaks in March and November. Regarding the contribution of each layer
40   to the total AOD (shown numerically labelled at the top axis of Figs. S2 (a) and (b)), the lower layer L_1 contributes more than 40% throughout the year, with the only exception of August. In wintertime (December, January and February), we observe a contribution $\geq 60\%$ of L_1 to the total AOD.
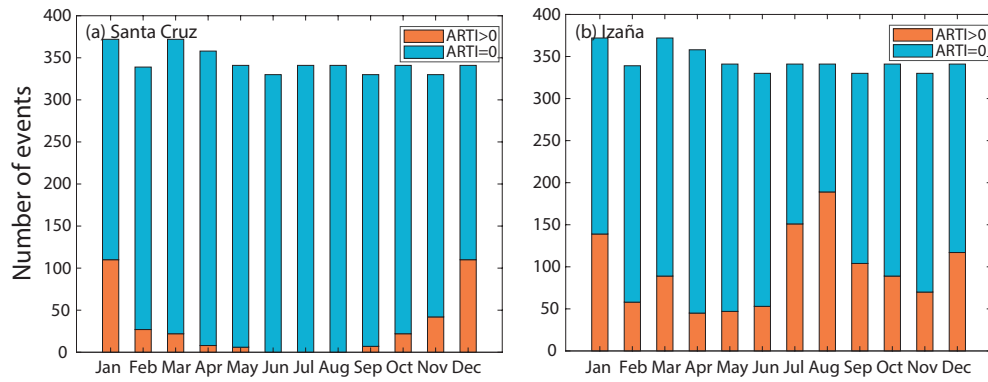
Figure S3. Cumulative histogram with the number of events with non-African origin (ARTI = 0 and with African origin (ARTI > 0) at (a) Santa Cruz level and (b) Izaña.

S3 Extinction profiles and vertical thermodynamic profiles for Saharan scenarios including RH

We have included in this Supplement a version of Fig. 2 that includes relative humidity (RH) (Fig. S4), which will be used
to detect the increase in the RH profile, with a maximum of 47% at 5.2 - 5.5 km height, as well as the mid-level clouds under
summer-SAL conditions detected after the peak in RH (45%-50%) associated with the SAL layer.
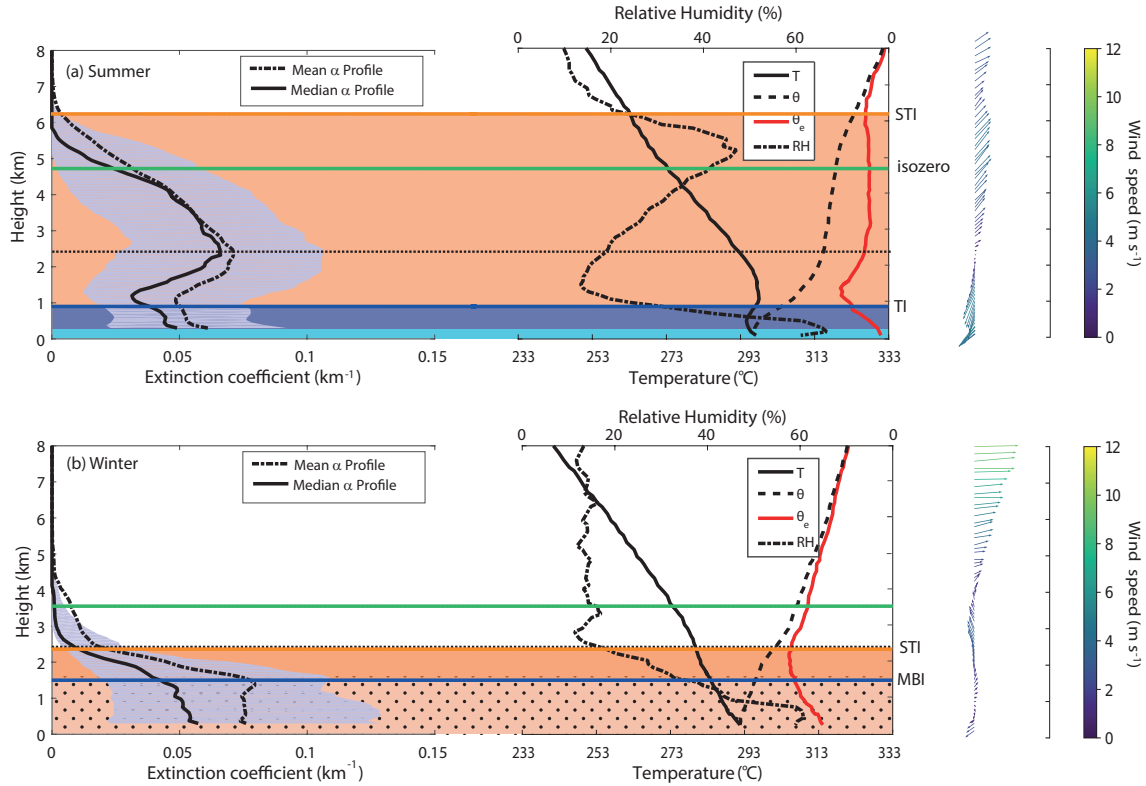
Figure S4. Extinction profiles (mean and median) and vertical profiles (median) of temperature (T), potential temperature (θ), equivalent
potential temperature (θ_e) and relative humidity (RH) for (a) summer-Saharan and (b) winter-Saharan scenarios. Black horizontal broken
line represents the IZO height. Blue and orange solid lines represent the MBI and STI top, respectively, detected from vertical soundings.
Green horizontal line indicates the average 0°C (isozero) level extracted from vertical soundings. The grey shaded area is bounded by the
20th and 80th percentile values of lidar total extinction at each level. 2D field of wind profiles with arrows (wind direction) and magnitude
are also presented on the right.

S4 Composites of average potential temperature from the NCEP/NCAR Reanalysis
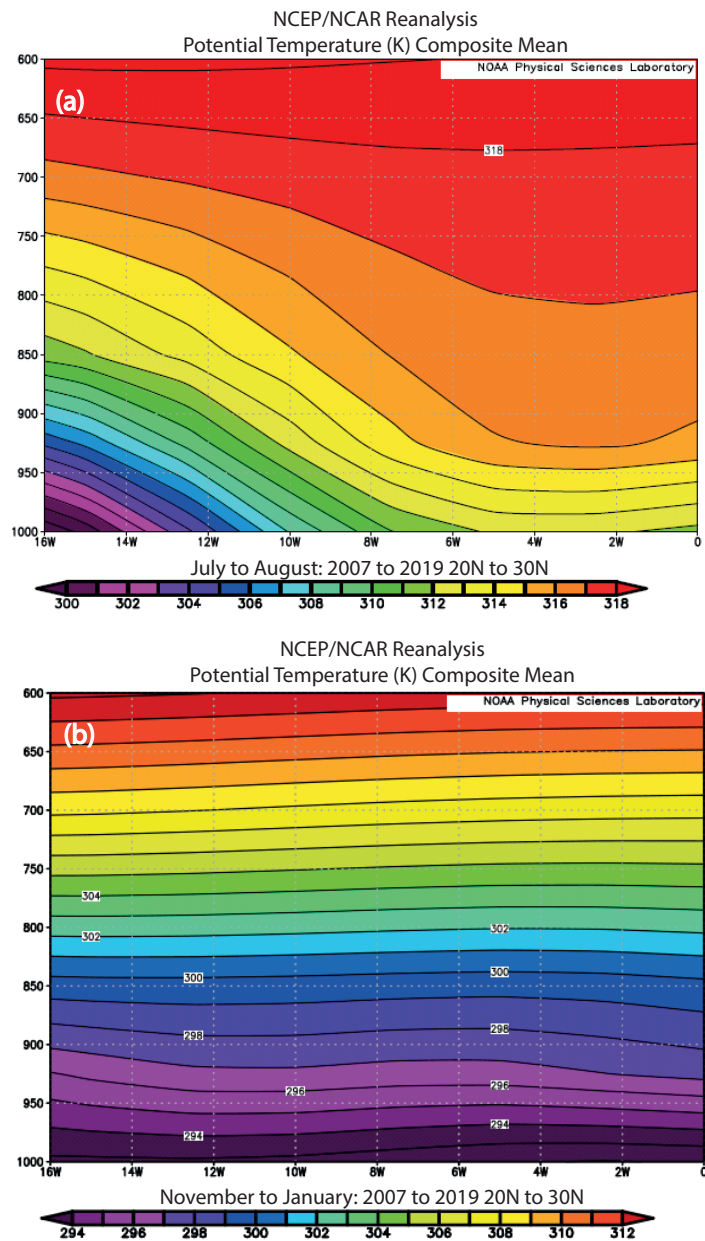
Figure S5. NCEP/NCAR Reanalysis composite (Kalnay et al., 1996) for Potential Temperature calculated between 20°-30°N and 16°W-0°W for (a) summer (July and August 2007-2019) and (b) winter (November-January 2007-2019).

## S5 Total attenuatted backscatter from the Cloud–Aerosol Lidar with Orthogonal Polarization (CALIOP)
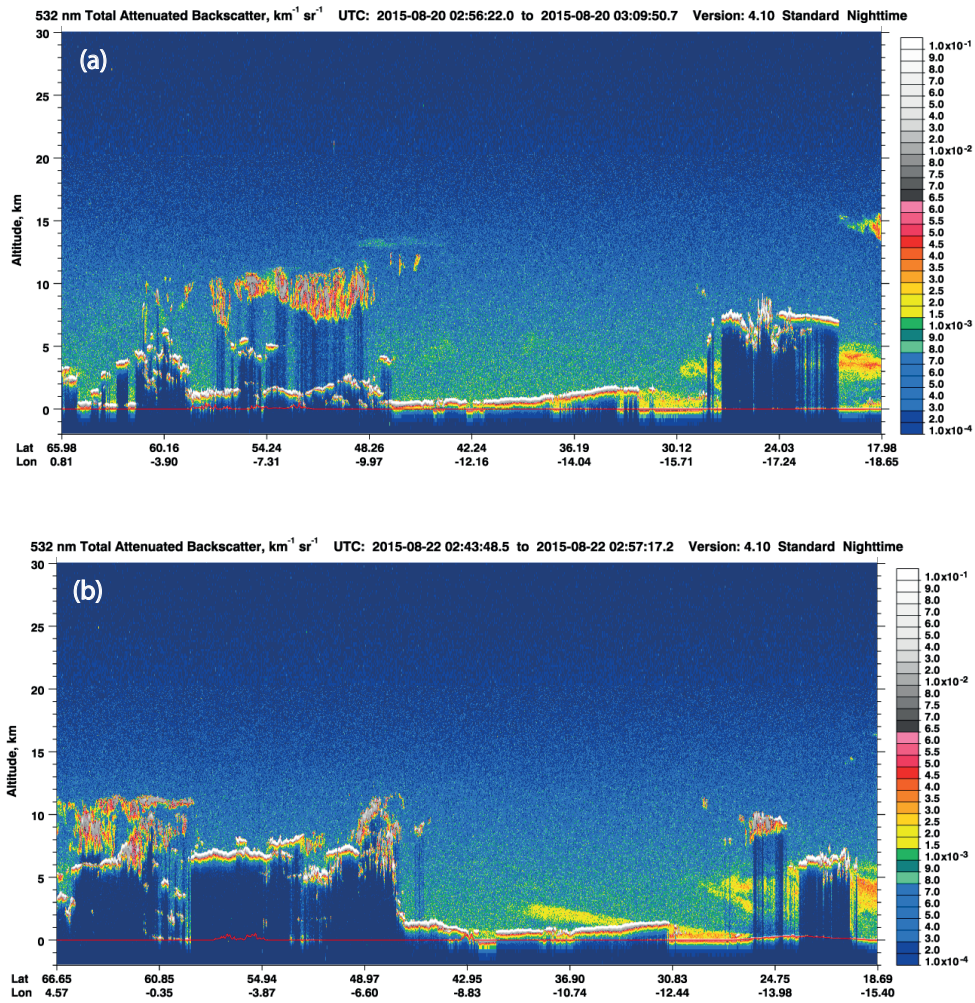
Figure S6. Total attenuated backscatter (in km^{-1} sr^{-1}) at 532 nm measured by CALIOP (Winker et al., 2009) for a portion of a nighttime scene on (a) 20 August 2015 and (b) 22 August 2015.
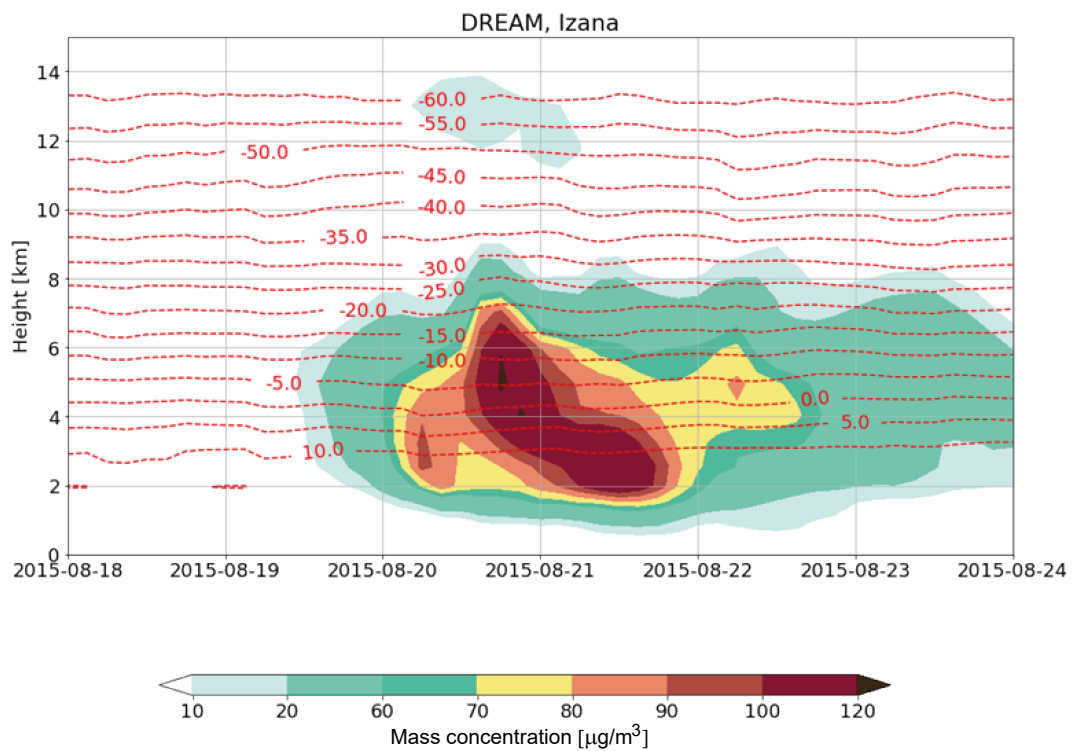
S6   Comparison of the extinction coefficient profiles retrieved with DREAM and MPL and DREAM mass concentration in a case study
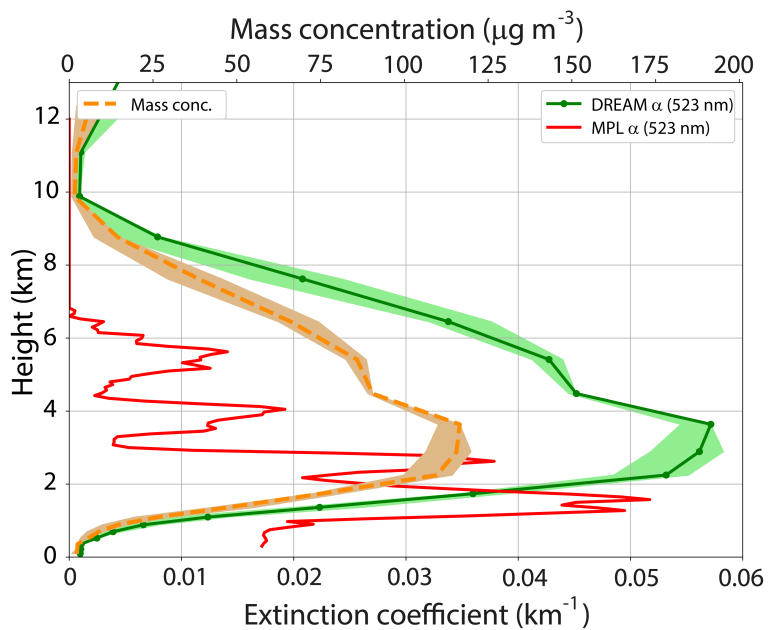
Figure S7. Extinction coefficient profiles (α in km^{-1}) retrieved with DREAM and MPL at 523 nm in addition to DREAM mass concentration (in μg m^{-3}) in a case study on August 21 10:54 UTC.

DREAM, Izana

Mass concentration [μg/m³]

Figure S8. Dust mass concentration (in μg m^{-3}) predicted by DREAM over Tenerife in the 5-day dust event between 19-24 August 2015.

References

Ansmann, A.: Ground-truth aerosol lidar observations: Can the Klett solutions obtained from ground and space be equal for the same aerosol case?, Appl. Optics, 45, 3367–3371, https://doi.org/10.1364/AO.45.003367, 2006.

Baars, H., Ansmann, A., Engelmann, R., and Althausen, D.: Continuous monitoring of the boundary-layer top with lidar, Atmos. Chem. Phys., 8, 7281–7296, https://doi.org/10.5194/acp-8-7281-2008, 2008.

Carrillo, J., Guerra, J. C., Cuevas, E., and Barrancos, J.: Characterization of the Marine Boundary Layer and the Trade-Wind Inversion over the Sub-tropical North Atlantic, Bound.-Layer Meteorol., 158, 311–330, https://doi.org/10.1007/s10546-015-0081-1, 2016.

Endlich, R., Ludwig, F., and Uthe, E.: An automatic method for determining the mixing depth from lidar observations, Atmos. Environ. (1967), 13, 1051 – 1056, https://doi.org/10.1016/0004-6981(79)90015-5, 1979.

Johnson, R., Ciesielski, P., and Kenneth, A.: Tropical inversions near the 0 °C level, J. Atmos. Sci., 53, 1838–1855, 1995.

Kalnay, E., Kanamitsu, M., Kistler, R., Collins, W., Deaven, D., Gandin, L., Iredell, M., Saha, S., White, G., Woollen, J., Zhu, Y., Chelliah, M., Ebisuzaki, W., Higgins, W., Janowiak, J., Mo, K. C., Ropelewski, C., Wang, J., Leetmaa, A., Reynolds, R., Jenne, R., and Joseph, D.: The NCEP/NCAR 40-Year Reanalysis Project, Bull. Am. Meteorol. Soc., 77, 437 – 472, https://doi.org/10.1175/1520-0477(1996)077<0437:TNYRP>2.0.CO;2, 1996.

Martucci, G., Matthey, R., Mitev, V., and Richner, H.: Comparison between Backscatter Lidar and Radiosonde Measurements of the Diurnal and Nocturnal Stratification in the Lower Troposphere, J. Atmos. Ocean. Technol., 24, 1231 – 1244, https://doi.org/10.1175/JTECH2036.1, 2007.

Rouault, M., Lee-Thorp, A. M., and Lutjeharms, J. R. E.: The Atmospheric Boundary Layer above the Agulhas Current during Alongcurrent Winds, J. Phys. Oceanogr., 30, 40 – 50, https://doi.org/10.1175/1520-0485(2000)030<0040:TABLAT>2.0.CO;2, 2000.

Von Engeln, A., Teixeira, J., Wickert, J., and Buehler, S. A.: Using CHAMP radio occultation data to determine the top altitude of the Planetary Boundary Layer, Geophys. Res. Lett., 32, https://doi.org/https://doi.org/10.1029/2004GL022168, 2005.

Wiegner, M., Emeis, S., Freudenthaler, V., Heese, B., Junkermann, W., Münkel, C., Schäfer, K., Seefeldner, M., and Vogt, S.: Mixing layer height over Munich, Germany: Variability and comparisons of different methodologies, J. Geophys. Res.-Atmos., 111, https://doi.org/https://doi.org/10.1029/2005JD006593, 2006.

Winker, D. M., Vaughan, M. A., Omar, A., Hu, Y., Powell, K. A., Liu, Z., Hunt, W. H., and Young, S. A.: Overview of the CALIPSO Mission and CALIOP Data Processing Algorithms, J. Atmos. Ocean. Technol., 26, 2310 – 2323, https://doi.org/10.1175/2009JTECHA1281.1, 2009.

Zhong, T., Wang, N., Shen, X., Xiao, D., Xiang, Z., and Liu, D.: Determination of Planetary Boundary Layer height with Lidar Signals Using Maximum Limited Height Initialization and Range Restriction (MLHI-RR), Remote Sens., 12, https://doi.org/10.3390/rs12142272, 2020.